



Evaluation of Fracture Toughness of Sandstone and Shale Using Digital Image Correlation

Vladyslav Kramarov¹ · Prathmesh Naik Parrikar¹ · Mehdi Mokhtari¹

Received: 28 January 2020 / Accepted: 4 June 2020
 © Springer-Verlag GmbH Austria, part of Springer Nature 2020

Abstract

Success of a hydraulic fracturing operation depends on the height and width of the induced fractures. One of the critical components controlling fracture size is fracture toughness of the formation. In this work, mode I fracture toughness of Berea Sandstone and Mancos Shale is measured by combining semi-circular bend test (SCB) and digital image correlation (DIC). Experiments were carried out in different notch orientations with respect to bedding. DIC is used to measure full-field displacements and to visualize and quantify fracture process zone (FPZ). Full-field displacements from DIC are utilized in Williams' series solution to extract critical stress intensity factor, or fracture toughness. Accuracy of measuring fracture toughness using DIC displacements depends on area of interest (AOI), field of view (FOV), and the number of terms of solution (N). A parametric study is conducted, allowing to choose an optimal set of these parameters for evaluation of fracture toughness in rock specimens. It is known that fracture toughness values obtained directly from the SCB test, using conventional maximum load method, are underestimated due to the effect of nonlinear behavior caused by the fracture process zone. FPZ length is considered as an increase in the effective crack length. Irwin's correction for effective crack length is utilized to measure fracture toughness values obtained directly from the SCB test that account for the fracture process zone. Fracture toughness values measured using DIC method and Irwin's correction method are in a good match for both Berea Sandstone and Mancos Shale. Both methods show higher fracture toughness for samples in arrester orientation. In addition, the results show that FPZ length in Berea Sandstone is much larger than in Mancos Shale.

Keywords Fracture toughness · Digital image correlation · Semi-circular bend test · Fracture process zone · Anisotropic rocks

List of Symbols

a_0	Initial notch length	K_{IC}^{APR}	Mode I apparent fracture toughness
a_{eff}	Effective notch length	K_{IC}^{DIC}	Mode I fracture toughness obtained from the DIC
AOI	Area of interest	K_{IC}^{IRW}	Mode I fracture toughness with Irwin's correction
B	Thickness of the sample	K_{II}	Mode II stress intensity factor
CTOD	Crack tip opening displacement	LEFM	Linear elastic fracture mechanics
DIC	Digital image correlation	MMTS	Modified maximum tangential stress
f_I, f_{II}, g_I, g_{II}	Known functions of a point k	N	Number of terms in solution
FEM	Finite element method	ν	Poisson's ratio
FOV	Field of view	r_k, θ_k	Polar coordinates of a point k
FPZ	Fracture process zone	r_y	Fracture process zone length
G	Shear modulus	R	Radius of the sample
K_I	Mode I stress intensity factor	SIF	Stress intensity factor
K_{IC}	Mode I fracture toughness	STD	Standard deviation
		T_x, T_y, R	Translation and rotation components in displacement equations
		u	Horizontal displacement fields captured by DIC

✉ Prathmesh Naik Parrikar
 prathmesh.naik-parrikar@louisiana.edu

¹ University of Louisiana At Lafayette, Lafayette, LA, USA

UCS	Uniaxial compressive strength
v	Vertical displacement fields captured by DIC
Y	Non-dimensional stress intensity factor

1 Introduction

Production of hydrocarbons from tight formations directly depends on the success of hydraulic fracturing operations. Most of the hydraulic fracturing is done on shales and tight sandstones, due to their low porosity and permeability. Since the 1940s, fracture initiation and propagation in these formations have been a subject of interest. Shales are sedimentary layered rocks and each layer has different mechanical properties. Various numerical models are built to simulate hydraulic fracturing. Parameters used for simulations are confining pressure, mechanical properties, fracture toughness, and mineralogy. Fracture toughness (K_{IC}), however, is often disregarded, and its effect considered negligible (Gokaraju et al. 2017; Thiercelin 1989). According to Barree et al. (2010), fracture height predictions in laminated formations are overestimated in comparison to results from microseismic analysis. In their work, Gokaraju et al. (2017) also showed that assigning standard values for K_{IC} leads to over-predicting of fracture height and underestimating of fracture width. It is obvious that obtaining correct fracture toughness values is critical for more accurate hydraulic fracturing simulation and design.

Fracture toughness is the ability of material to resist propagation of preexisting cracks or flaws. For mode I, fracture toughness is denoted as K_{IC} and is considered to be an intrinsic property of material, independent of the size of the specimen. However, studies have shown that fracture toughness can vary greatly with respect to specimen size and configuration (Bazant et al. 1991; Chang et al. 2002; Anderson 2005; Ayatollahi and Akbardoost 2012; Al-Shayea 2005). In this case, it is referred to as critical stress intensity factor (SIF) or the apparent fracture toughness of material (Ayatollahi and Akbardoost 2012). The dependency of the apparent on specimen size is caused by the presence of fracture process zone (FPZ) at the crack tip (Ayatollahi and Akbardoost 2012). Effects of the FPZ on fracture toughness are discussed later in this section. Theoretically, measuring intrinsic fracture toughness using equations derived based on linear elastic fracture mechanics (LEFM) requires an infinitely large sample to eliminate the effect of the FPZ. Researchers determined that with an increase in specimen size, apparent fracture toughness eventually reaches a consistent value which can be considered as the K_{IC} of material. These specimen size values, however, are rather large; Ayatollahi and Akbardoost (2013a, b) determined that the K_{IC} of Ghorveh marble should be measured using specimen radius of 1500 mm for the semi-circular bend test, while Karihaloo

(1999) stated that to eliminate the effect of the FPZ in concrete, minimum specimen length for the three-point bend test can be over 700 mm depending on the specimen configuration. These extreme specimen sizes make standard laboratory fracture toughness tests rather complicated; for this reason, researchers created models to estimate FPZ length of specimens and use this value to obtain inherent fracture toughness of materials that is independent of specimen size.

Fracture process zone (FPZ) is a zone of microcracking that surrounds a tip of the crack and it develops with an increase in load (Bazant et al. 1991; Lim et al. 1994a, b; Dong et al. 2017; Yu et al. 2019). This phenomenon causes inelastic softening deformation of the sample; thus it cannot be accurately described by the linear elastic fracture mechanics (LEFM). Guo et al. (1993) concluded that the FPZ is the reason for the difference between energy release and energy dissipation rates during loading. For that reason, standard LEFM fracture toughness equations that are based on peak load (P_{max}) are not efficient in estimating fracture toughness of samples that are affected by the FPZ. Different methods to measure K_{IC} accounting for the FPZ have been proposed. Irwin (1961) proposed to use the term “effective notch length” which included initial notch length and plastic zone size. He stated that plastic zone size can be measured as a function of stress intensity factor (SIF) and yield stress of the sample. This method of measuring plastic zone size cannot be used for geologic materials because the term “yield stress” is not applicable to them. Schmidt (1980) proposed a model that estimates length of the FPZ as a function of critical SIF and tensile strength of the rock. Ayatollahi and Akbardoost (2012) proposed a modified Schmidt’s model, adding a non-singular Williams’s series solution term into the equation. However, laminated rocks exhibit different tensile strength values with respect to bedding orientation; for this reason, implementation of these methods requires a larger number of samples and might result in a higher cost. Meredith (1989) proposed a “ductility correction factor” that is proportional to how linearly the material behaves under loading conditions. However, even samples from the same formation cannot always be accurately described by a single correction factor, due to their high degree of heterogeneity. Based on studies by Bazant et al. (1986) and Karihaloo (1995), Ayatollahi and Akbardoost (2012) presented a modified maximum tangential stress (MMTS) model that estimates FPZ length for a specimen of any size. This model is used to predict FPZ length of an infinitely large specimen which is then applied in the K_{IC} equation to measure the inherent fracture toughness. This model, however, requires a large number of preliminary experiments on specimens with different size to obtain constant coefficients that are used in the equation. Wei et al. (2016) combined the acoustic emission method with finite element method (FEM) to detect and measure FPZ which was used to correct K_{IC} values. Acoustic

emission can be used to detect FPZ but is not applicable to accurately measure its size and shape, while FEM results strongly depend on input parameters and boundary conditions. Methods listed above only estimate FPZ length but do not provide a way to measure it exactly. In this work, FPZ is visualized and quantified using digital image correlation.

The International Society of Rock Mechanics suggests several fracture toughness tests like chevron bend test, short rod test, cracked chevron notched Brazilian disk test (Kuruppu et al. 2013; Fowell 1995). One of a more recently suggested tests is semi-circular bend test (SCB), and it has been used in a number of works to measure mode I and mode II fracture toughness of different formations due to its simplicity (Kuruppu and Chong 1984, 2012; Lim et al. 1994a, b; Aliha et al. 2012; Lee et al. 2015). Another advantage of the SCB test is the ability to test samples in all principal notch orientations with respect to bedding. It was shown that K_{IC} values in shales are sensitive with respect to changes in bedding (Wang et al. 2017; Lee et al. 2015; Forbes Inskip et al. 2018). The equation used to measure fracture toughness is derived based on linear elastic fracture mechanics (LEFM) which assumes that tested material behaves according to LEFM. However, geologic materials tend to show nonlinear behavior as they approach peak load. It has been reported that K_{IC} values obtained from conventional fracture toughness tests, including the SCB test, are underestimated due to nonlinear behavior of the sample that is caused by the presence of the FPZ (Tutluoglu and Keles 2010; Wei et al. 2016). Dyskin (1997) stated that the inherent fracture toughness presumed by the LEFM can be achieved only if the process zone is infinitesimal. Zhang et al. (2015) used digital image correlation to determine that the crack starts propagating before reaching the peak load which implies that traditional approach to measuring K_{IC} of rocks using the SCB test might be inefficient.

Digital image correlation (DIC) is a non-contact measurement technique, in which pixel intensity is measured before and after deformation (Nath and Mokhtari 2018). This allows for the visualization of a full-field displacement during testing. DIC has been used in fracture mechanics, where Williams' expansion series are combined with an over-deterministic least square method extract parameters like SIF and fracture toughness from displacement fields (McNeill et al. 1987; Gao et al. 2015; Yoneyama et al. 2007; Zhang and He 2012). The results showed a good match with conventional methods for measuring these parameters. Accuracy of this method depends on parameters like area of interest (AOI) of DIC, field of view (FOV) and the number of terms in solution (N). Mokhtarishirazabad et al. (2016) have conducted a parametric study in which the effect of these parameters was tested. They determined that accurate measurement of SIF can be obtained using FOV from $4 \times 4 \text{ mm}^2$ to $10 \times 10 \text{ mm}^2$, AOI that covers about 25% of the notch, and N of 12 or

greater when used on linear elastic materials like PMMA. Ayatollahi and Nejati (2011) conducted a convergence study using finite element over-deterministic method, determining that term A_1 that is related to mode I SIF converges at N of 5. Williams' series solution was designed for perfectly brittle materials, and for this reason, this method of measuring SIF is considered well established for PMMA and other materials that show almost perfect linear elastic behavior. On the other hand, the accuracy of this method for materials that exhibit large FPZ is relatively unknown. At this time, few works have been published on analyzing fracture mechanics of geologic materials. Lin and Labuz (2013) presented a method of measuring FPZ and crack tip opening displacement (CTOD) of Berea Sandstone using horizontal displacement fields. Gao et al. (2015) measured the dynamic fracture toughness of Laurentian Granite. Quasi-static fracture toughness of rocks using DIC has not been thoroughly studied, and the effect of parameters of the solution has not been examined.

In this work, DIC is integrated with the SCB test to measure mode I fracture toughness of Berea Sandstone and Mancos Shale. These samples were selected because they represent two distinct classes of formations that undergo hydraulic fracturing: sandstone and shale. Experiments were conducted on specimens with different notch orientation with respect to bedding to evaluate fracture toughness in different directions. First, the effect of parameters of DIC solution to measure fracture toughness is studied, allowing to choose for optimal AOI, N and FOV. Once optimal parameters are selected, full-field displacements obtained by the DIC are utilized to calculate fracture toughness using Williams' expansion series and over-deterministic least square method. Then, FPZ length is quantified using DIC, and Irwin's approach is utilized to obtain fracture toughness values from the SCB test that account for nonlinear behavior. Two sets of values are then compared, showing a good match for both Berea Sandstone and Mancos Shale samples.

2 Theory

2.1 Semi-Circular Bend Test

SCB test is used to determine mode I fracture toughness. During the mode I test, the tensile stress field develops ahead of the crack tip. K_I , or mode I stress intensity factor (SIF), is a term that describes the stress field state around the tip of the notch. Under quasi-static conditions and pure mode I deformation, the critical value of the SIF is the mode I fracture toughness (Kuruppu et al. 2013). For the semi-circular bend test, K_{IC} can be measured using Eq. 1 (Lim et al. 1993; Kuruppu et al. 2013).

$$K_{IC} = \frac{Y' P_{\max} \sqrt{\pi a_0}}{2RB}, \quad (1)$$

where P_{\max} is peak load, R is radius, B is thickness, a_0 is initial notch length, S is support span and Y' is non-dimensional stress intensity factor defined as (Kuruppu et al. 2013):

$$Y' = -1.297 + 9.516\left(\frac{S}{2R}\right) - \left(0.47 + 16.457\left(\frac{S}{2R}\right)\right) \times \frac{a_0}{2R} + \left(1.071 + 34.401\left(\frac{S}{2R}\right)\right) \left(\frac{a_0}{2R}\right)^2.$$

Schematics of the SCB test are shown in Fig. 1.

Because of the presence of the FPZ in quasi-brittle materials, this equation will underestimate the value of the inherent fracture toughness (Ayatollahi and Akbardoost 2012; Tutluoglu and Keles 2011; Wei et al. 2016). In this case, K_{IC} is the apparent fracture toughness and will be denoted as K_{IC}^{APR} , and unlike the inherent fracture toughness, it is size dependent.

Presence of the FPZ results in a nonlinear relationship between stress intensity factors and load, making LEFM equations that are based on peak load insufficient in measuring the inherent fracture toughness (Anderson 2005).

Because presence of nonlinear behavior affects fracture toughness results, Irwin (1961) proposed to use a term “effective notch length” to correct the values. For the SCB test, fracture toughness solution with Irwin’s correction becomes:

$$K_{IC}^{IRW} = \frac{Y' P_{\max} \sqrt{\pi a_{\text{eff}}}}{2RB}, \quad (2)$$

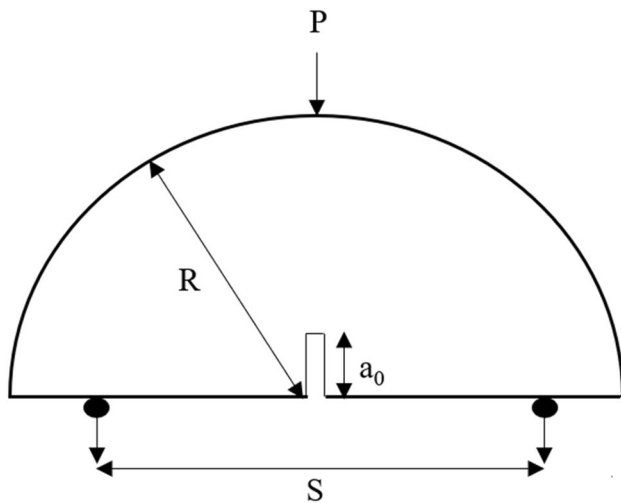


Fig. 1 Schematics of the SCB test

$$a_{\text{eff}} = a_0 + r_y, \quad (3)$$

where r_y is plastic zone size. For rocks, r_y is the length fracture process zone (FPZ), because nonlinear behavior in geologic materials is caused by subcritical cracking and not by plasticity (Lim et al. 1994a, b; Anderson 2005). r_y is

determined using DIC and used to correct fracture toughness using Eq. 2. Subsequently, non-dimensional stress intensity factor Y' is calculated using a_{eff} . Fracture toughness calculated using Eq. 2 is the inherent fracture toughness.

2.2 Digital Image Correlation

Digital image correlation (DIC) is a non-contact measurement technique, in which pixel intensity is measured before and after deformation (Nath and Mokhtari 2018). This allows for visualization of a full-field displacement during rock testing. Using speckling technique, groups of pixels are united into subsets. After material undergoes deformation, the subset from the reference image is matched with a subset from the deformed image. After subsets are matched, relative displacement between the center of a subset from reference image and the center of the subset from deformed image is calculated by DIC. This allows for a full-field displacement and strain calculations. Equations 4 and 5 are used to measure displacement of each subset. Figure 2 depicts a scheme of digital image correlation principle (Gao et al. 2015).

$$x' = x_0 + \Delta x + u + \frac{\partial u}{\partial x} \Delta x + \frac{\partial u}{\partial y} \Delta y, \quad (4)$$

$$y' = y_0 + \Delta y + v + \frac{\partial v}{\partial x} \Delta x + \frac{\partial v}{\partial y} \Delta y. \quad (5)$$

2.3 DIC Solution Using Full-Field Displacement

The horizontal (u) and vertical (v) displacement of any point near the crack tip can be described using Williams’ series solution shown in Eqs. 6 and 7 (Sanford and Dally 1979; McNeill et al. 1987; Gao et al. 2015; Yoneyama et al. 2007; Zhang and He 2012).

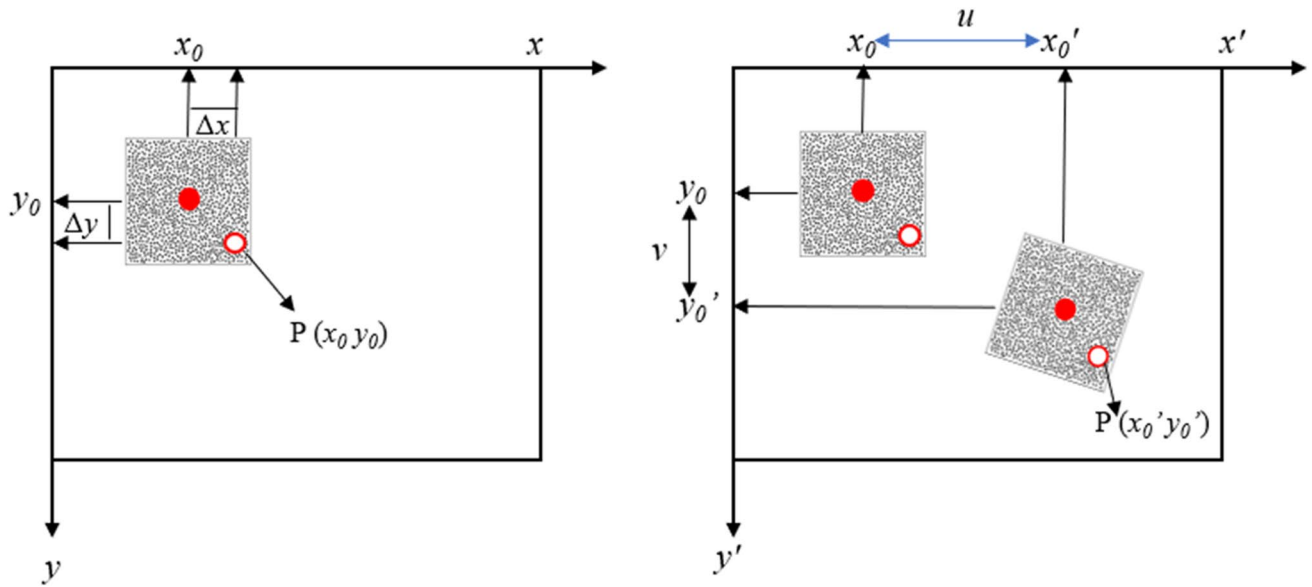


Fig. 2 Scheme of digital image correlation principle

$$u = \sum_{n=1}^N \frac{A_{In}}{2G} r^{\frac{n}{2}} \left\{ \cos\left(\frac{n}{2}\theta\right) - \frac{n}{2} \cos\left(\frac{n}{2}-2\right)\theta + \left\{\frac{n}{2} + (-1)^n \cos\left(\frac{n}{2}\right)\theta\right\} \right. \\ \left. - \sum_{n=1}^N \frac{A_{In}}{2G} r^{\frac{n}{2}} \left\{ \kappa \sin\left(\frac{n}{2}\theta\right) - \frac{n}{2} \sin\left(\frac{n}{2}-2\right)\theta + \left\{\frac{n}{2} - (-1)^n\right\} \times \sin\left(\frac{n}{2}\theta\right)\right\} + T_x - Ry, \right. \quad (6)$$

$$v = \sum_{n=1}^N \frac{A_{In}}{2G} r^{\frac{n}{2}} \left\{ \kappa \sin\left(\frac{n}{2}\theta\right) + \frac{n}{2} \sin\left(\frac{n}{2}-2\right)\theta - \left\{\frac{n}{2} + (-1)^n \sin\left(\frac{n}{2}\right)\theta\right\} \right. \\ \left. - \sum_{n=1}^N \frac{A_{In}}{2G} r^{\frac{n}{2}} \left\{ -\kappa \cos\left(\frac{n}{2}\theta\right) - \frac{n}{2} \cos\left(\frac{n}{2}-2\right)\theta + \left\{\frac{n}{2} - (-1)^n\right\} \times \cos\left(\frac{n}{2}\theta\right)\right\} + T_y + Rx, \right. \quad (7)$$

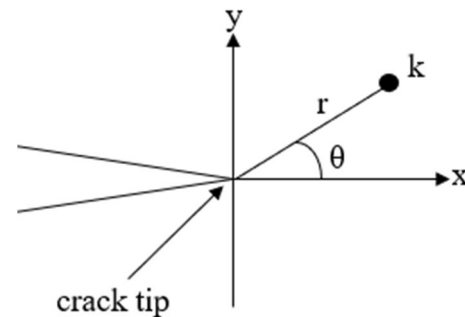
where G is shear modulus, ν is poisson's ratio, r and θ are polar coordinates of the point with respect to crack tip and n is the number of terms in solution. A_{I1} and A_{II1} are unknowns that depend on loading conditions. Because plain stress conditions require extremely thin samples, for rocks, it is easier to achieve conditions that are similar to plain strain. For this reason, plain strain κ of $3-4\nu$ is used. Terms T_x , T_y , and R are added to account for horizontal and vertical translation, and rotation, respectively (Yoneyama et al. 2007; Zhang and He 2012).

Terms A_{I1} and A_{II1} can be related to mode I (K_I) and mode II (K_{II}) stress intensity factors through Eqs. 8 and 9.

$$A_{I1} = \frac{K_I}{\sqrt{2\pi}}, \quad (8)$$

$$A_{II1} = -\frac{K_{II}}{\sqrt{2\pi}}. \quad (9)$$

Equation 10 is a condensed form of Eq. 6 and 7 for a particular point k with polar coordinates r_k , θ_k (shown in Fig. 3), where f_I , f_{II} , g_I , and g_{II} are known functions of a point k .


 Fig. 3 Coordinates of a crack tip and point k (after Yoneyama et al. 2007)

$$\begin{aligned}
u_k &= \sum_{n=1}^N (A_{In} f_{In}(r_k, \theta_k)) - \sum_{n=1}^N (A_{IIIn} f_{IIIn}(r_k, \theta_k)) + T_x - Ry_k, \\
v_k &= \sum_{n=1}^N (A_{In} g_{In}(r_k, \theta_k)) - \sum_{n=1}^N (A_{IIIn} g_{IIIn}(r_k, \theta_k)) + T_y + Rx_k.
\end{aligned}
\quad (10)$$

These equations can be rewritten in a matrix form to account for multiple points at the time. Assuming that M is a number of points and N is a number of terms used, Eq. 11 is obtained.

$$h = b \times \Delta, \quad (11)$$

where

$$h = \begin{bmatrix} u_1 \\ \vdots \\ u_m \\ v_1 \\ \vdots \\ v_m \end{bmatrix}, \dots, \dots b = \begin{bmatrix} f_{I1}(r_1, \theta_1) & \cdots & -f_{II1}(r_1, \theta_1) & \cdots & 1 & 0 & -y_1 \\ \vdots & \ddots & \vdots & \ddots & \vdots & \vdots & \vdots \\ f_{I1}(r_M, \theta_M) & \cdots & -f_{II1}(r_M, \theta_M) & \cdots & 1 & 0 & -y_M \\ g_{I1}(r_1, \theta_1) & \cdots & -g_{II1}(r_1, \theta_1) & \cdots & 0 & 1 & x_1 \\ \vdots & \ddots & \vdots & \ddots & \vdots & \vdots & \vdots \\ g_{I1}(r_M, \theta_M) & \cdots & -g_{II1}(r_M, \theta_M) & \cdots & 0 & 1 & x_M \end{bmatrix}, \Delta = \begin{bmatrix} A_{I1} \\ \vdots \\ A_{II1} \\ T_x \\ T_y \\ R \end{bmatrix}.$$

Equation 12 shows a least square solution to solve for the unknown Δ and evaluate A_{In} and A_{IIIn} .

$$[\Delta] = [b]^T [b]^{-1} [b]^T [h]. \quad (12)$$

Once optimum parameters of DIC solution (AOI, N , and FOV) are selected, full-field displacements obtained from the DIC are used in William's series solution to measure mode I SIF of the samples. Subsequently, full-field displacements taken at the peak load, provide critical value of the SIF, denoted in this work as K_{IC}^{DIC} . In this work, only mode I fracture toughness is discussed. It is important to note that the length of the FPZ is not incorporated in the DIC solution, i.e., original crack tip location is used in the calculations of fracture toughness using DIC displacements.

3 Methodology and Experimental Setup

3.1 Methodology

Fracture toughness in different notch orientations with respect to bedding is investigated. For sedimentary rocks four principal orientations are:

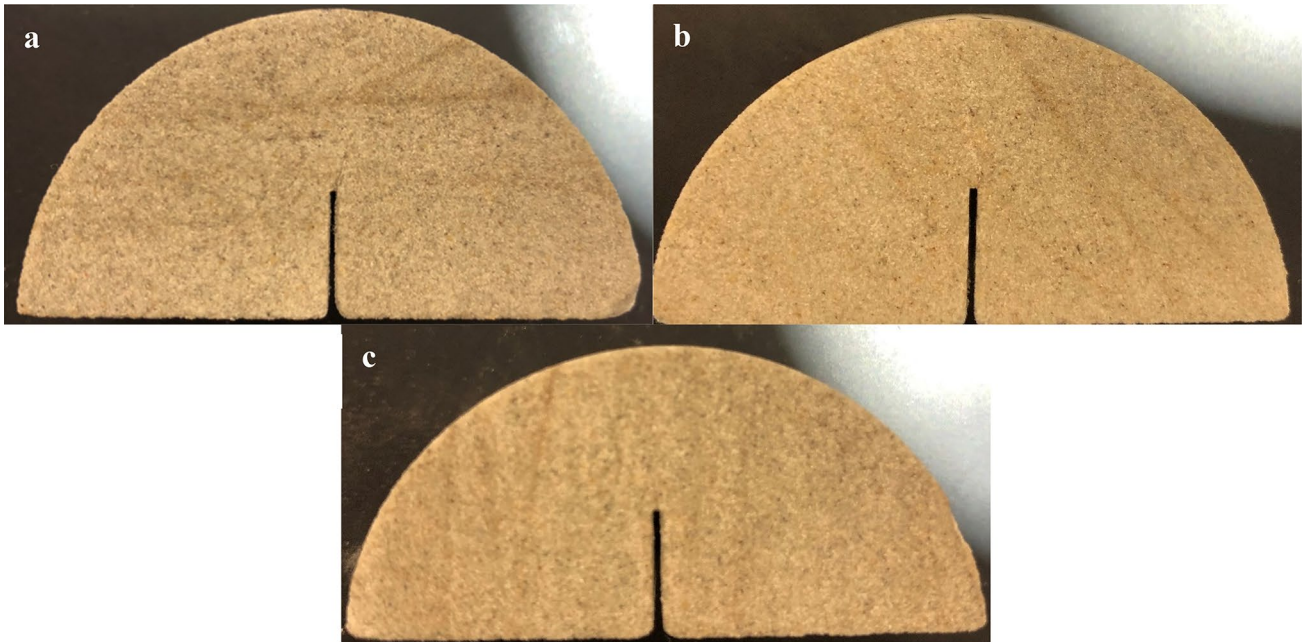


Fig. 4 Berea Sandstone samples in different orientations. Figure 3a—arrested, Fig. 3b—45°, Fig. 3c—short transverse. Water was applied to samples to amplify the contrast between laminations

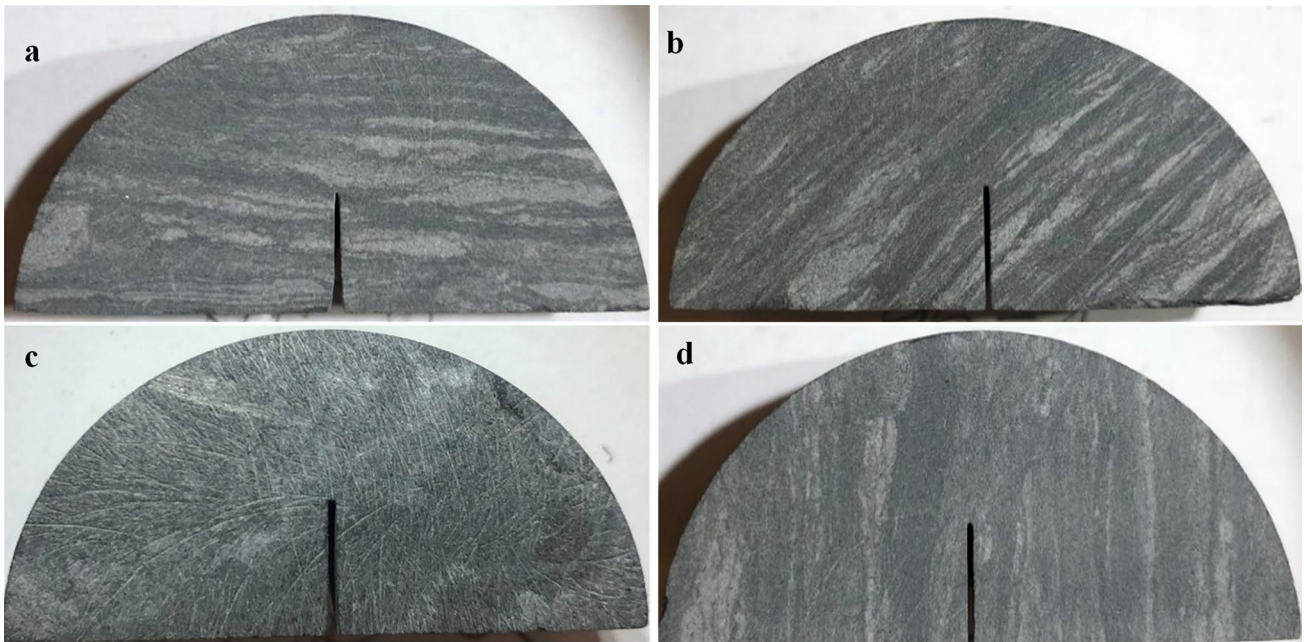


Fig. 5 Mancos Shale samples in different orientations. Figure 4a—arrested, Fig. 4b—45°, Fig. 4c—divided, Fig. 4d—short transverse

Table 1 Dimensions and peak load of Berea Sandstone samples

Berea SS						
Sample	D (mm)	B (mm)	R (mm)	a (mm)	S (mm)	P_{\max} (N)
AR-1	50.5	24.1	23.9	9.4	37.9	562
AR-2	50.5	25.4	23.6	8.9	37.9	772
AR-3	50.5	23.9	24.6	9.9	37.9	586
ST-1	50.8	24.6	24.9	9.7	37.9	383
ST-2	50.5	24.4	23.4	10.4	37.9	309
45-1	50.5	24.1	25.1	11.7	37.9	436
45-2	50.3	24.1	23.4	9.4	37.9	427

Table 2 Dimensions and peak loads of Mancos Shale samples

Mancos Shale						
Sample	D (mm)	B (mm)	R (mm)	a (mm)	S (mm)	P_{\max} (N)
AR-1	50.5	28.4	23.4	9.4	37.9	1423
AR-2	37.5	26.4	17.5	6.4	28.1	872
AR-3	37.5	26.2	17.5	7.1	28.1	1138
ST-1	50.5	27.9	24.9	9.7	37.9	925
ST-2	50.5	28.2	23.9	9.9	37.9	783
45-1	50.8	28.4	24.6	10.4	37.9	956
45-2	50.5	27.9	24.9	9.7	37.9	996
D-1	37.3	25.9	17.0	7.6	28.1	547
D-2	37.6	25.1	18.8	7.9	28.1	721
D-3	37.3	24.4	17.3	7.1	28.1	529

- arrester (AR)—bedding orientation is perpendicular with respect to notch;
- short transverse (ST)—bedding orientation is parallel with respect to notch;
- 45° (45)—bedding orientation is 45° with respect to notch;
- divider (D)—front of the notch is perpendicular to bedding plane;

In this study, 10 Mancos Shale outcrop samples were tested in all four principal orientations. Eight Berea Sandstone outcrop samples were tested in three orientations—arrester, short transverse, and 45°. Cylindrical core samples were obtained from Kocurek Industries. Samples were manufactured using a circular table saw. An extremely thin blade (0.178 mm thick) was used to notch the specimens. Notch thickness was approximately 0.190 for all samples. Figures 4, 5 show Berea Sandstone and Mancos Shale samples in all tested orientations. Dimensions, span lengths, and peak loads of all tested samples are listed in Tables 1 and 2.

It is important to note that outcrop samples might not accurately represent fracture toughness of the rock in reservoir conditions which was shown by Al-Shayea (2002)

William's series solution used in the DIC solution (Eqs. 6 and 7) requires shear modulus and Poisson's ratio of the specimen. Uniaxial compressive strength (UCS) test was conducted to measure Young's modulus (E) and Poisson's ratio of the samples. Shear modulus was estimated using Eq. 13 (Bazant et al. 1991; Nejati et al. 2019).

$$G = \frac{E}{2(1 + \nu)}. \quad (13)$$

Due to limited sample availability, the UCS test was conducted only on samples with bedding orientation perpendicular to the applied load. In this case, the measured E and ν correspond to the arrester orientation of the specimen. For Mancos Shale, G was then estimated to be eight GPa, while ν was measured to be 0.15. Ramos et al. (2018) conducted a study, in which they analyzed sonic wave velocities of Mancos Shale in different bedding orientations. In their work, Thomsen Parameter γ , which is a measure of shear modulus anisotropy, was calculated to be 0.122 which agrees well with Chandler et al (2016). Using γ and shear wave velocities provided in their work, G of Mancos Shale was estimated to be 7.70 GPa for samples in short transverse orientation, 7.73 GPa in for samples in 45° orientation, and 9.90 GPa for samples in divider orientation. From literature, Poisson's ratio varies mostly between 0.10 and 0.2 for different bedding orientations (Kennedy 2011; Chandler et al. 2016; Mikhaltsevitch et al. 2016). Because ν has a much weaker effect on the results from DIC solution than G , a single value of 0.15 for all samples is used.

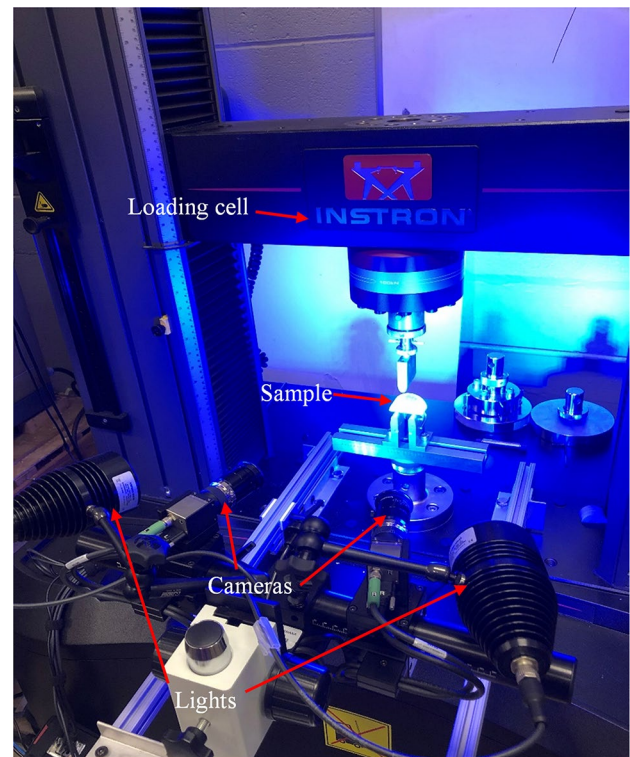


Fig. 6 Experimental setup. Loading cell, sample, cameras, and lights are marked with red arrows

For Berea Sandstone, ν was measured to be 0.3 and G was estimated to be 2.5 GPa. Ramos et al. (2017) showed that there is only about 4% shear wave anisotropy (subsequently, shear modulus anisotropy) in Berea Sandstone at no confining stress. For Mancos Shale, G values in arrester, short transverse, and 45° orientations are close, while G in divider orientation is significantly larger. Because Berea Sandstone samples are not tested in divider orientation, and there is only 4% of Shear Modulus anisotropy, a single value of G of 2.5 GPa is used for all the samples. Similarly, because of a relatively lower degree of anisotropy, and weaker effect on the DIC solution, a single value of ν equal to 0.3 is used.

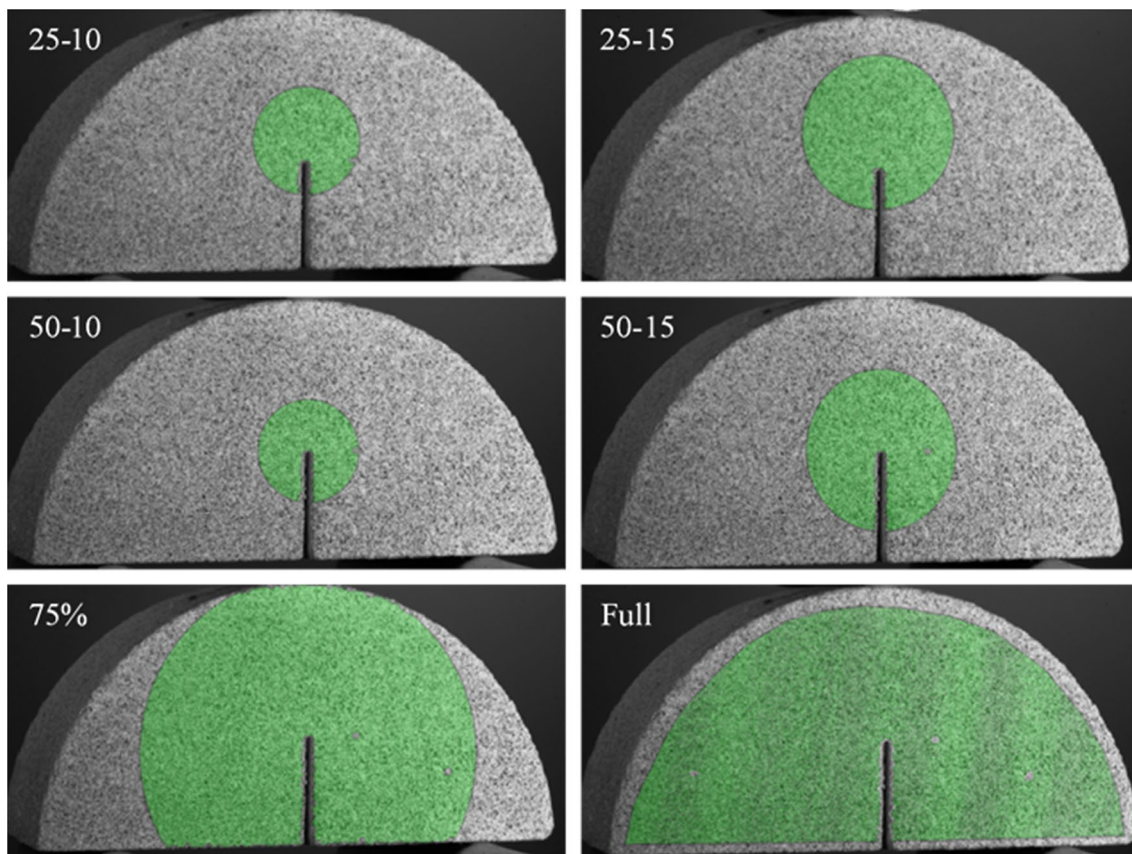
3.2 Experimental Setup

Experimental setup is shown on Fig. 6. For the SCB test, Instron 5982 Universal Testing System with a load cell capacity of 100 kN is used. To ensure that the tests are conducted in quasi-static regime, a displacement rate of the cross-head is 0.05 mm/min. The DIC hardware and analysis parameters are listed in Table 3 according to DIC Good Practices Guide for digital image correlation (2018). Subset size/step size combinations of 50/25, 40/20, 30/15 and 25/12 were used. All combinations gave results within 1%; however, computational time varied by 2–3 times. For

Table 3 Hardware and analysis parameters of DIC

Hardware parameters		Analysis parameters	
Camera	Stereo, 12 M	Software	Aramis professional
Image resolution	4096 × 3000	Subset size	50 pixels (0.650 mm)
Lens	Schneider 50 mm	Step size	25 pixels (0.325 mm)
Field of view*	52 × 39 mm ²	Subset shape function	Quadratic
Stereo-angle	25°	Strain filtering	Spatial
SOD	35 cm	Area of interest*	~ 1000 mm ²
Acquisition rate	2 Hz		
Patterning technique	Spraying		
Pattern size	~ 5–10 pixels		

List of parameters listed is taken from DIC good practices guide

**Fig. 7** Tested areas of interest

that reason, subset size/step size combination of 50/25 was used. Field of view of $52 \times 39 \text{ mm}^2$ and area of interest of $\sim 1000 \text{ mm}^2$ were used for most of the samples. Detailed analysis of effect of FOV and AOI is presented in Sect. 4.

4 Results and Discussion

4.1 Effect of Area of Interest

Effect of area of interest was studied on two Berea SS and two Mancos Shale samples. Effect of AOI was studied using FOV of $52 \times 39 \text{ mm}^2$ and N of 10. Areas of interest were chosen based on the size and location with respect to notch.

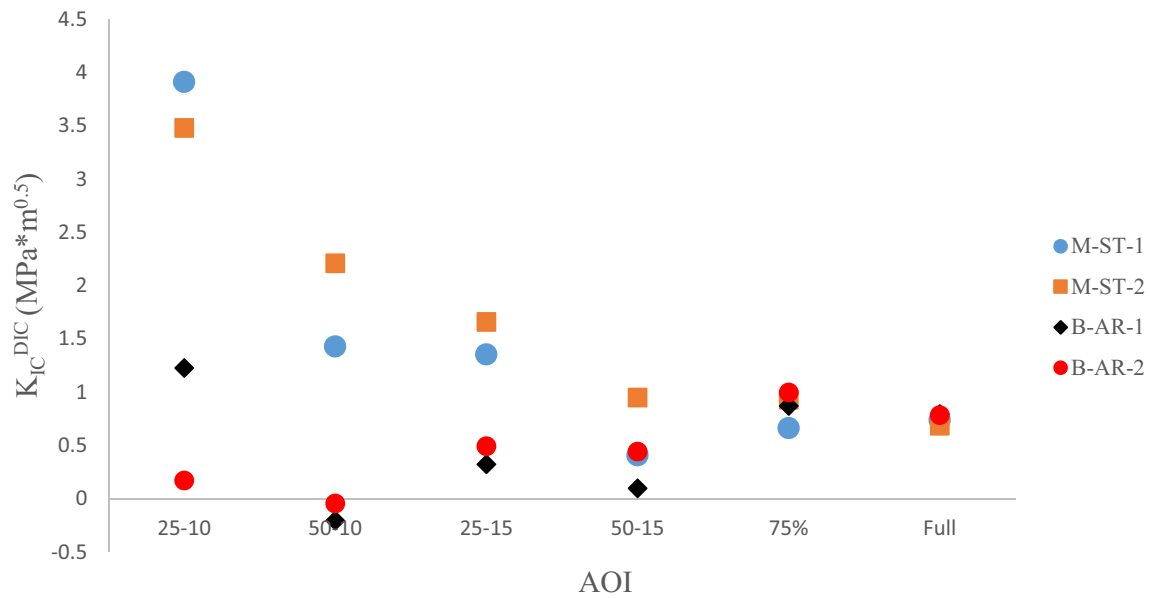


Fig. 8 K_{IC}^{DIC} values measured using tested AOI's. M-ST-1 is enlarged for better visualization at "Full" AOI

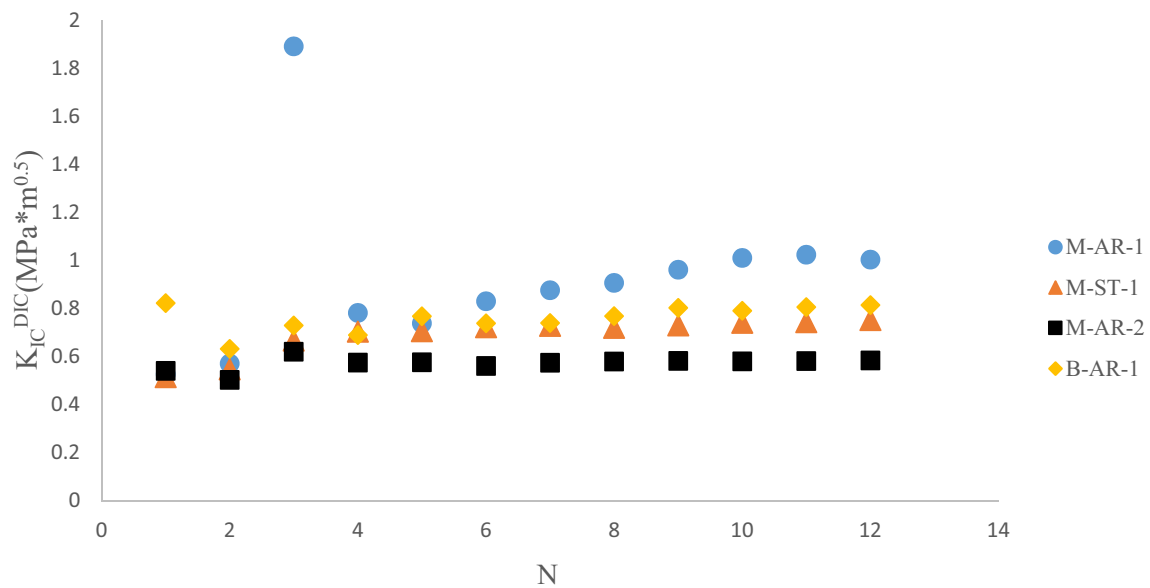


Fig. 9 K_{IC}^{DIC} values calculated using different number of terms (N)

For better size accuracy, all AOI's were created in circular shape. Six AOI's were tested, where:

- 25–10—diameter of AOI is 10 mm; notch tip is one-fourth of diameter;
- 50–10—diameter of AOI is 10 mm; notch tip is a half of diameter;
- 25–15—diameter of AOI is 15 mm; notch tip is one-fourth of diameter;
- 50–15—diameter of AOI is 15 mm; notch tip is a half of diameter;
- 75%—AOI covers approximately 75% of the whole sample, including some contact points and edges;
- full—AOI covers full area of a sample, excluding contact points and edges.

Tested AOI's are highlighted in green in Fig. 7. Figure 8 shows calculated K_{IC}^{DIC} values for different AOI's.

Table 4 K_{IC}^{DIC} values measured at different FOV's

Field of view (mm ²)	K_{IC}^{DIC} (MPa × m ^{0.5})	K_{IC}^{IRW} (MPa × m ^{0.5})	Resolution (mm/pixel)
12×9 AR-4	0.158	0.538	0.0029
28×21—AR-3	0.680	0.780	0.0068
52×39—AR-2	0.791	0.820	0.0126

Figure 8 shows that at a small AOI around the notch tip results in vastly different K_{IC}^{DIC} for each experiment. Analytical solution tends to either grossly overestimate, or underestimate values of fracture toughness. In previous works, it was shown that if the notch is 25% of the size of AOI, stress intensity factors of PMMA obtained are reasonable (Mokhtarishirazabad et al. 2016). In this work, material exhibits larger nonlinear behavior and sharp displacement gradients; for that reason, small AOI around the tip of the crack fails to give reasonable answer. As the AOI increases, K_{IC}^{DIC} values for all four samples tested start to converge. Both “75%” and “Full” AOI show reasonable results, but for “Full” AOI, a better match between samples in the same orientation is observed. In addition, displacement fields at the contact points with loading rods are not described by equations used in analytical solution. Softer rocks could undergo larger bending at contact points, which could affect the results. Finally, because a subset-based method was used, the values obtained at the edges of speckle pattern tend to be misleading. For these reasons, it is recommended to use an area of interest that captures a full sample, excluding contact points and edges.

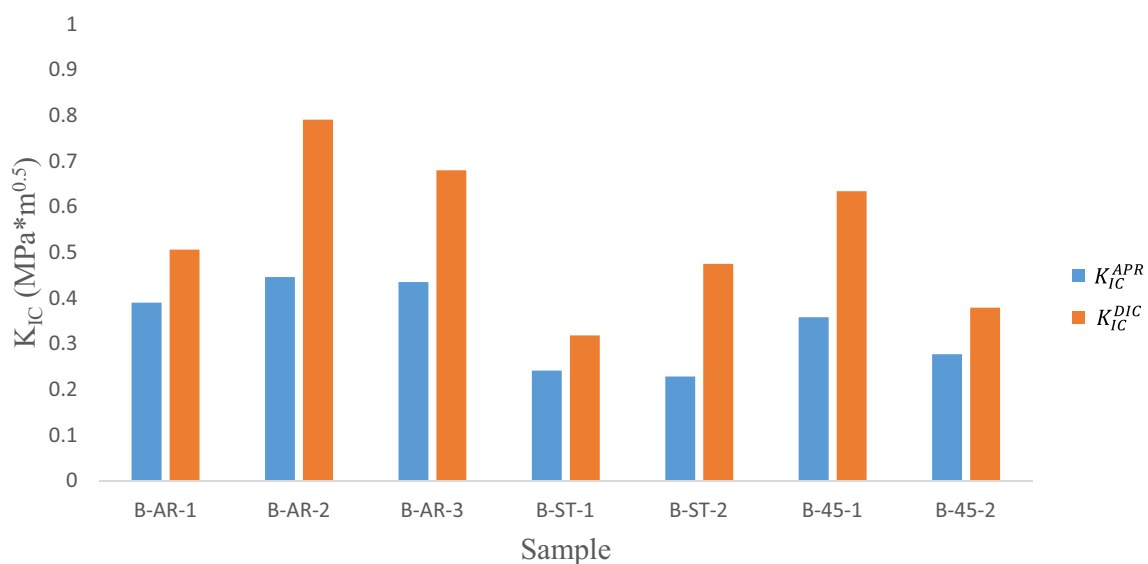
4.2 Effect of Number of Terms of Solution

The effect of number of terms (N) on K_{IC}^{DIC} values for two Berea SS and two Mancos Shale samples has been tested. To evaluate the effect of N , “Full” AOI and FOV of 52×39 mm² were used. The results are shown in Fig. 9. At N values between 1 and 8, numerical solution tends to underestimate the results. At N values of 10 and more, solution shows good convergence. For all results, $N = 10$ was used for both accurate results and fast computational time. In some cases, K_{IC}^{DIC} values show slight increase after $N = 10$; this increase, however, is much smaller (~0.1%) than for N values between 1 and 8, thus, it can be neglected. “Full” area of interest and field of view of 52×39 mm² were used.

4.3 Effect of Field of View

3 Fields of view were tested—12×9 mm², 28×21 mm² and 52×39 mm² on three Berea SS samples. All FOV's were centered at the crack tip. All FOV's were centered at the crack tip. “Full” AOI and N of 10 were used to evaluate the effect of FOV. Results are shown in Table 4, where they are compared to K_{IC}^{IRW} values (discussed later in this section).

Effect of FOV is similar to effect of AOI. Small FOV around the crack tip does not give reasonable results due to sharp displacement gradients in that region. Both 28×21 mm² and 52×39 mm² give results that are close to K_{IC}^{IRW} values; however, 28×21 mm² FOV does not capture full size of the sample. In some cases, FPZ can extend beyond 28×21 mm² which would make it impossible

**Fig. 10** Comparison of K_{IC}^{APR} and K_{IC}^{DIC} values obtained for Berea Sandstone samples (except for sample AR-4)

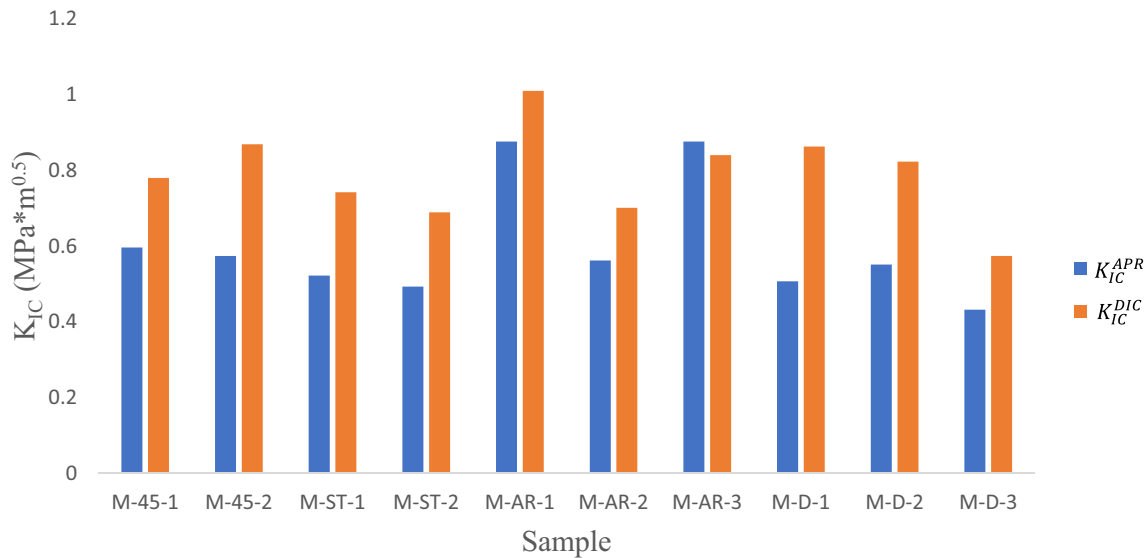


Fig. 11 Comparison of K_{IC}^{APR} and K_{IC}^{DIC} values obtained for Mancos Shale samples

Table 5 Comparison of K_{IC}^{APR} and K_{IC}^{DIC} for all samples

	K_{IC}^{APR} (MPa \times m ^{0.5})	K_{IC}^{DIC} (MPa \times m ^{0.5})
B-AR-1	0.390	0.506
B-AR-2	0.446	0.791
B-AR-3	0.435	0.680
B-ST-1	0.241	0.318
B-ST-2	0.228	0.475
B-45-1	0.358	0.634
B-45-2	0.277	0.379
M-45-1	0.596	0.780
M-45-2	0.574	0.869
M-ST-1	0.522	0.742
M-ST-2	0.493	0.689
M-AR-1	0.876	1.010
M-AR-2	0.562	0.701
M-AR-3	0.876	0.840
M-D-1	0.507	0.863
M-D-2	0.551	0.823
M-D-3	0.432	0.574

to correct fracture toughness values for the FPZ. The downside of using large FOV is loss of resolution. In-plane movement accuracy of DIC is 0.02% of a pixel size, while measured displacements range from 1×10^{-3} mm to 1.5×10^{-1} mm. For FOV of 52×39 mm², the measuring error is 2.5×10^{-5} mm which is still within acceptable range. However, using larger FOV can cause more significant errors in displacements. For these reasons, FOV of

52×39 mm² is optimal for samples with diameter ranging from 38 to 51 mm.

Based on the presented results, it becomes clear that selecting the right combination of these three parameters is essential for the accuracy of the results; if one of the parameters is not selected properly, the results might be grossly overestimated or underestimated and inconsistent.

4.4 Comparison of Fracture Toughness Values

Figure 10 represents a comparison of the apparent fracture toughness calculated using Eq. 1 (K_{IC}^{APR}) and fracture toughness obtained from the DIC solution (K_{IC}^{DIC}). DIC solution tends to give higher values than Eq. 1. The average difference between two sets of values is 35%. It was calculated using Eq. 14.

$$\frac{1}{n} \sum_{i=1}^n \text{abs} \left(\left(\frac{K_{IC}^{DIC} - K_{IC}^{APR}}{K_{IC}^{DIC}} \right) \right). \quad (14)$$

Figure 11 represents a comparison between K_{IC}^{APR} and K_{IC}^{DIC} values for Mancos Shale. DIC solution tends to give higher results; using Eq. 14, the average difference between two sets of values is 28%.

Exact fracture toughness values for both Berea Sandstone and Mancos Shale are listed in Table 5.

4.5 Analysis of Nonlinear Behavior

It was shown that LEFM equations used to measure K_I and fracture toughness (Eq. 1) are accurate only if there is a

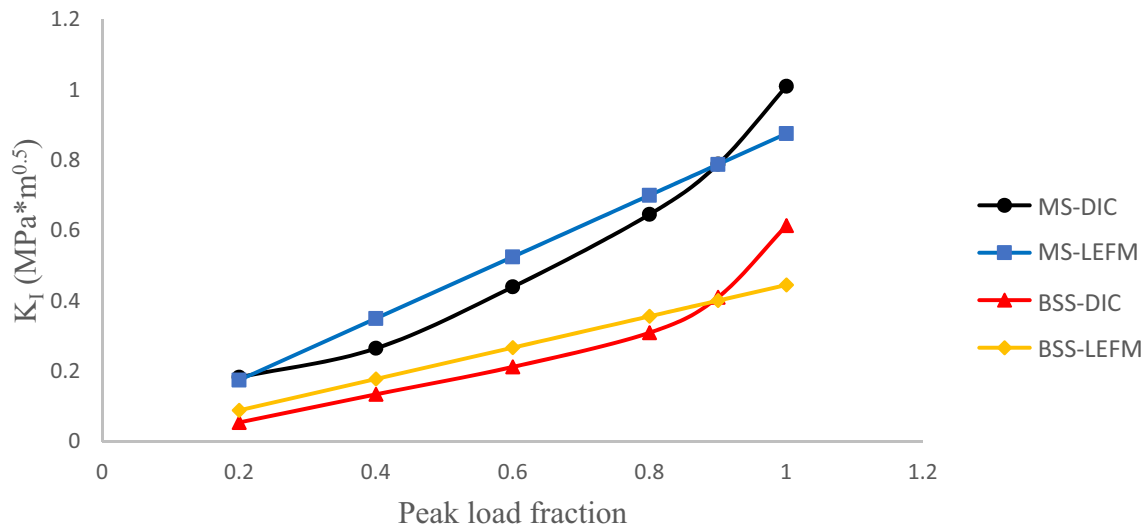


Fig. 12 Relationship between K_I and load for two tested samples

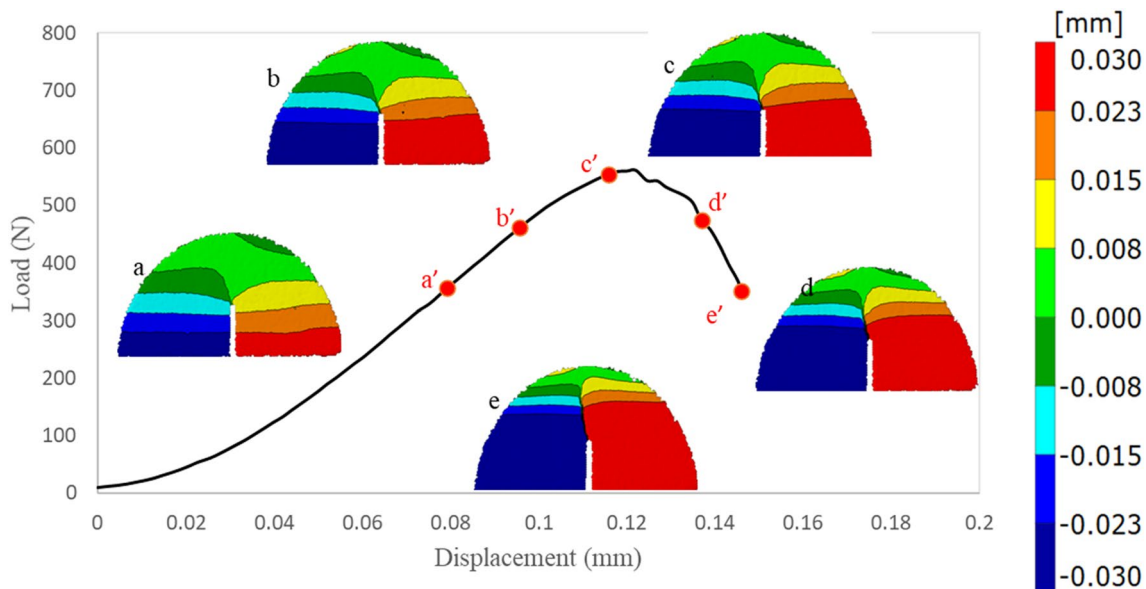


Fig. 13 Development of FPZ of a Berea Sandstone sample during testing

perfectly linear relationship between SIF and load (Anderson 2005). According to Anderson (2005), if nonlinear behavior is present, the value of K_I is underestimated as the sample approaches peak load. It is also known that semi-circular bend test tends to underestimate fracture toughness values due to larger FPZ (Chang et al. 2002; Tutluoglu and Keles 2010; Wei et al. 2016). Because FPZ causes a nonlinear relationship between SIF and load, its' presence can be determined by analyzing the relation between these variables. Figure 12 shows a comparison between K_I values measured using Eq. 1 taken from the LEFM, and the DIC solution for

one Berea SS and one Mancos Shale sample. K_I is measured at 20, 40, 60, 80, 90, and 100% of peak load.

Although DIC solution is designed for perfectly brittle materials, it still shows nonlinear behavior between 80 and 90% of peak load for both samples. It becomes clear that values obtained directly from the SCB test using peak load are underestimated and need to be corrected for the effect of the FPZ.

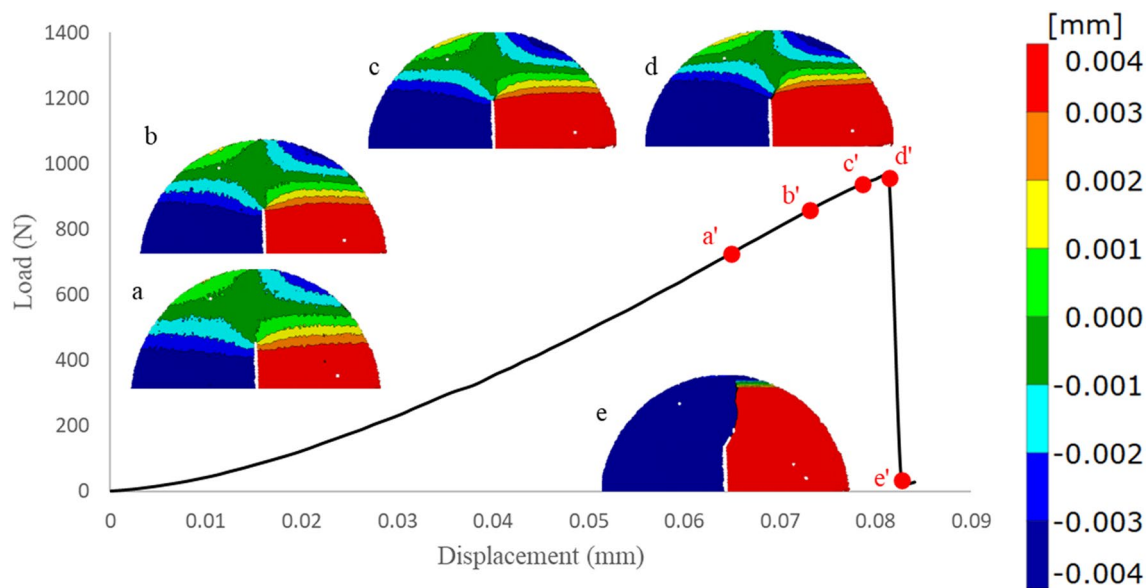


Fig. 14 Development of the FPZ of a Mancos Shale sample during testing

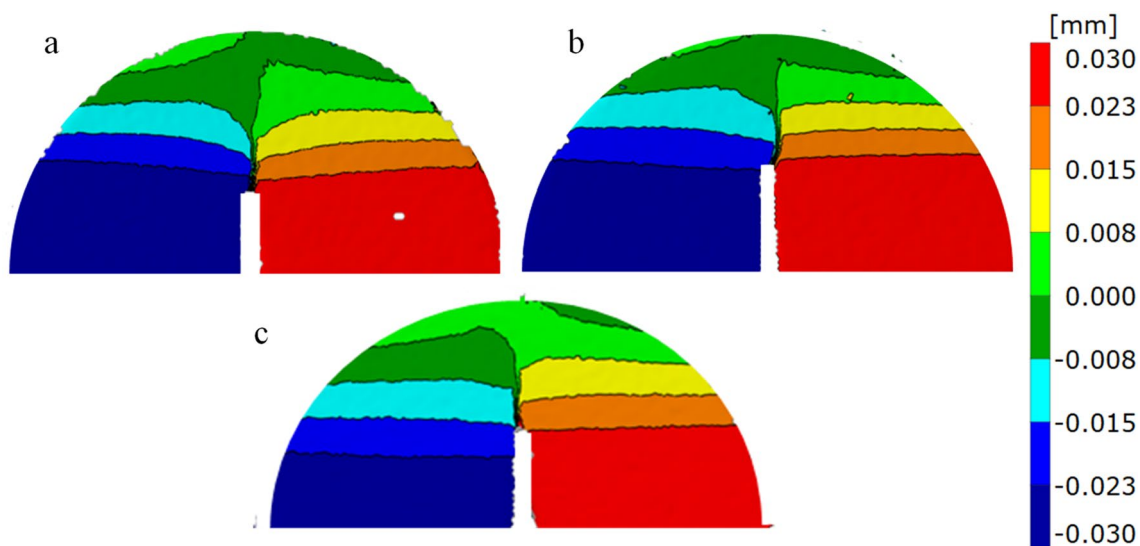


Fig. 15 Fully developed FPZ of Berea Sandstone samples in different orientations. Figure 14a—arrester, Fig. 14b—45°, Fig. 14c—short transverse. Displacement scale is provided to the right

4.6 Development of Fracture Process Zone

DIC is used to visually track development of the FPZ during loading. Figures 13, 14 show load versus cross-head displacement curves obtained from the Universal Testing System for one Berea Sandstone and one Mancos Shale sample, respectively. Five full-field u displacement images are plotted on the graph (a–e) with corresponding load values (a'–e'). Negative displacements ($-u$) are directed to the left of the image, positive displacements (u) are directed to the right of the image. Scale range is different for both samples,

because Berea Sandstone undergoes larger u displacements. Peak load of Berea Sandstone sample is 562 N, while for Mancos Shale, the peak load is 956 N. FPZ in Berea starts developing at 461 N which is 82% of peak load. Image “c” shows fully developed FPZ at 554 N which is 99% of peak load. After the sample reaches peak load, the load does not drop rapidly, and a complete failure of the sample is not observed as seen on image “d”. A possible interpretation is that FPZ causes softening behavior of the sample which results in a more ductile rather than a completely brittle failure. Finally, image “e” shows the sample at 350 N which

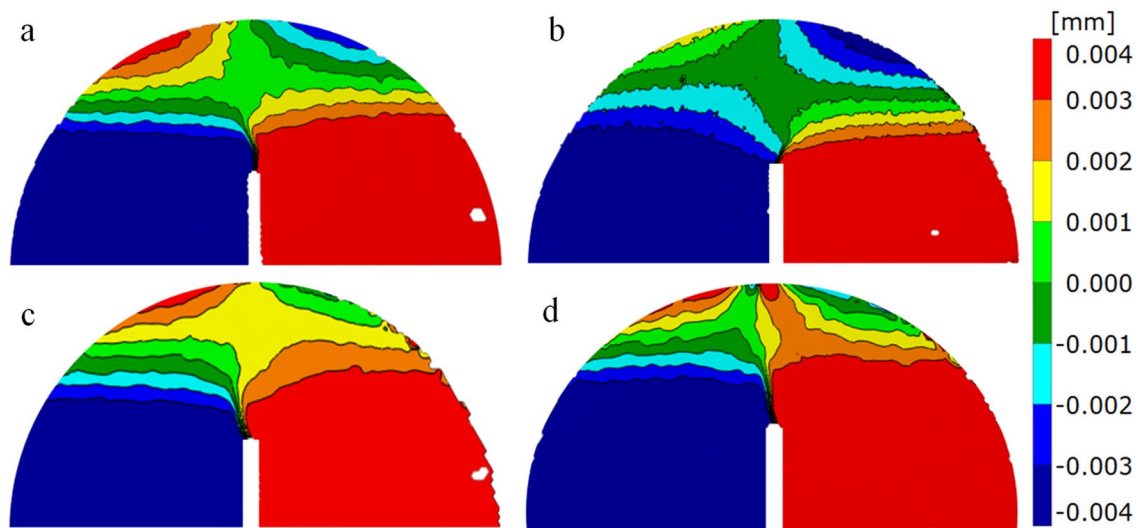


Fig. 16 Fully developed FPZ of Mancos Shale samples in different orientations. Figure 15a—arrester, Fig. 15b—45°, Fig. 15c—short transverse, Fig. 15d—divider. Displacement scale is provided to the right

is at 62% of post-peak load. The sample is yet to fail completely and a sharp drop in load is not observed. Mancos Shale sample exhibits a different behavior and FPZ development. Images “a” and “b” are taken at 75% of peak load and 90% of peak load, respectively, showing no FPZ. FPZ starts to develop at 937 N, which is 98% of peak load as presented on image “c”. Fully developed FPZ is seen on image “d”, which is taken at 99% of peak load. After reaching peak load, Mancos Shale sample exhibits different behavior. The load drops sharply, and the sample fails completely as shown on image “e”. A possible interpretation is that the FPZ and inelastic softening deformation in Mancos Shale is much smaller than in Berea Sandstone which leads to a more brittle failure of the sample.

Fully developed FPZ for Berea Sandstone and Mancos Shale samples in samples with different notch orientation is represented in Figs. 15, 16, respectively. Different scale range was chosen, allowing for better visualization of FPZ in Mancos Shale samples. FPZ. None of the samples show a completely straight FPZ. For both formations, samples with 45° notch orientation with respect to bedding show large deviation of FPZ towards the bedding angle. A possible explanation to this is that microcracks along bedding planes get activated which causes deviation of FPZ.

4.7 Quantification of FPZ and CTOD

To accurately measure FPZ size, parallel horizontal sections at are plotted at different heights and u displacement is measured across the length of the sections as shown on Fig. 17. Y-axis shows u displacements and X-axis shows the length of the section at which the displacements are plotted. Section

length is 17 mm and is measured starting from the left side of the image. Negative displacements ($-u$) are directed to the left; positive displacements (u) are directed to the right. Crack tip is located at $X=8$ mm and is marked with a red dot.

Analyzing horizontal section $Y=0.05$ mm (right above the tip of the notch), a rapid change in displacement at $X=8$ mm is seen. This “jump” is caused by the FPZ. This rapid change in displacement is seen for curves starting at $Y=0.05$ mm to $Y=5.60$ mm. The location of the “jump” is different due to deviation of the FPZ. Finally, at $Y=6.70$ mm, the curve is smooth with no rapid change in displacement. This is considered to be the end of FPZ (Lin and Labuz 2013).

To measure CTOD, two points, 2 mm apart, are plotted on the horizontal section right above the tip of the notch (a and b) (Lin and Labuz 2013). The change in distance between these two points is CTOD. In this case CTOD is 0.030 mm as shown in Fig. 16. In-depth analysis of CTOD and development of cohesive zone model is outside the scope of this work.

Measured length of the FPZ’s and CTOD’s for each sample are listed in Table 6. Both FPZ and CTOD of Berea Sandstone are much larger than of Mancos Shale. Presence of a larger FPZ leads to a higher degree of nonlinearity during testing. No clear relation between FPZ size and notch orientation with respect to bedding is seen. Table 6 also includes length of the FPZ as a fraction of initial notch length (a_0). On average, length of the FPZ is about 49% of initial notch length for Berea Sandstone and more than 26% of initial notch length for Mancos Shale. It is clear that such

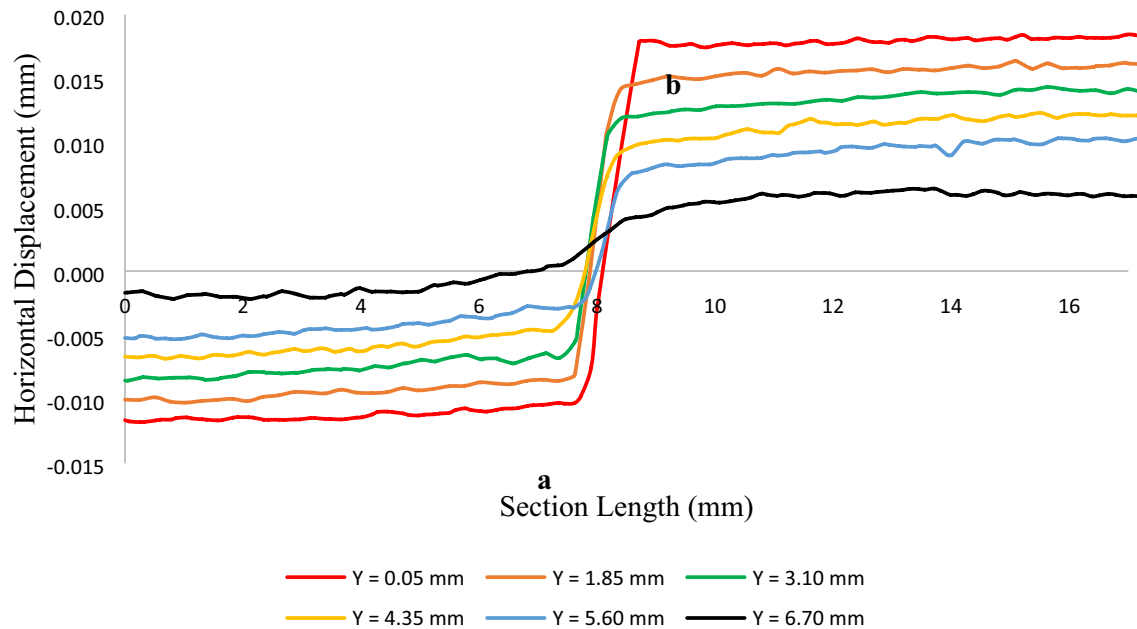


Fig. 17 Displacements across plotted horizontal sections for sample B-ST-2. Displacements at points (a, b) are used to calculate CTOD

large FPZ length cannot be neglected in fracture toughness calculations.

Methods listed in the Sect. 1 only provide estimations of the r_y and they require either additional data, like tensile strength of the rock, or a large number of experiments conducted on specimens with different size. DIC, on the other hand, provides the ability to physically observe FPZ and quantify its' length for each sample independent of its size. Moreover, it requires no additional data, making this method simpler, and possibly more reliable. Finally, DIC shows that FPZ length can be different in specimens of the same size that are taken from the same formation.

4.8 Corrected Fracture Toughness Values

FPZ length was utilized to calculate “effective notch length” (a_{eff}). Corrected fracture toughness values (K_{IC}^{IRW}) were calculated using Eq. 2. Figure 18 shows a comparison between K_{IC}^{APR} , K_{IC}^{IRW} and K_{IC}^{DIC} for Berea SS samples. Similarly, Fig. 19 shows the same comparison for Mancos Shale.

The average difference between K_{IC}^{IRW} and K_{IC}^{DIC} is measured using Eq. 14 by plugging K_{IC}^{IRW} instead of K_{IC}^{APR} . For Berea Sandstone, the average difference is 10.5%, while originally it was 35%; for Mancos Shale samples, the average difference is 9.6%, while originally it was 28%. In both cases, an improvement in relative matching accuracy is seen; this improvement is larger for Berea SS because it exhibits larger nonlinear deformation. Mancos Shale samples exhibit more brittle behavior and can be better described by

Table 6 FPZ length and CTOD for each sample

	Sample	FPZ (mm)	FPZ/ a_0	a_{eff} (mm)	CTOD (mm)
Berea sandstone	B-AR-1	3.6	0.383	13.0	0.045
	B-AR-2	6.0	0.674	14.9	0.051
	B-AR-3	4.8	0.485	14.7	0.043
	B-ST-1	4.0	0.412	13.7	0.032
	B-ST-2	6.7	0.644	17.1	0.030
	B-45-1	4.8	0.410	16.5	0.039
	B-45-2	4.2	0.447	13.6	0.034
	Mean	4.9	0.494	14.8	0.039
	STD	1.11	0.118	1.53	0.008
Mancos shale	M-AR-1	0.8	0.085	10.2	0.006
	M-AR-2	1.6	0.250	8.00	0.005
	M-AR-3	1.8	0.254	8.90	0.009
	M-ST-1	3.2	0.330	12.9	0.008
	M-ST-2	3.5	0.354	13.4	0.009
	M-45-1	2.0	0.192	12.4	0.008
	M-45-2	1.9	0.196	11.6	0.008
	M-D-1	2.7	0.355	10.3	0.009
	M-D-2	3.5	0.443	11.4	0.010
	M-D-3	1.5	0.211	8.60	0.009
	Mean	2.3	0.267	10.8	0.008
	STD	0.93	0.104	1.87	0.002

the LEFM—for this reason, an improvement in matching accuracy is smaller. Both cases, however, prove that nonlinear deformation affects results of the SCB test and that the apparent fracture toughness values underestimate values of the inherent fracture toughness. On average, $K_{\text{IC}}^{\text{APR}}$ is 43% lower than $K_{\text{IC}}^{\text{IRW}}$ for Berea Sandstone; for Mancos shale,

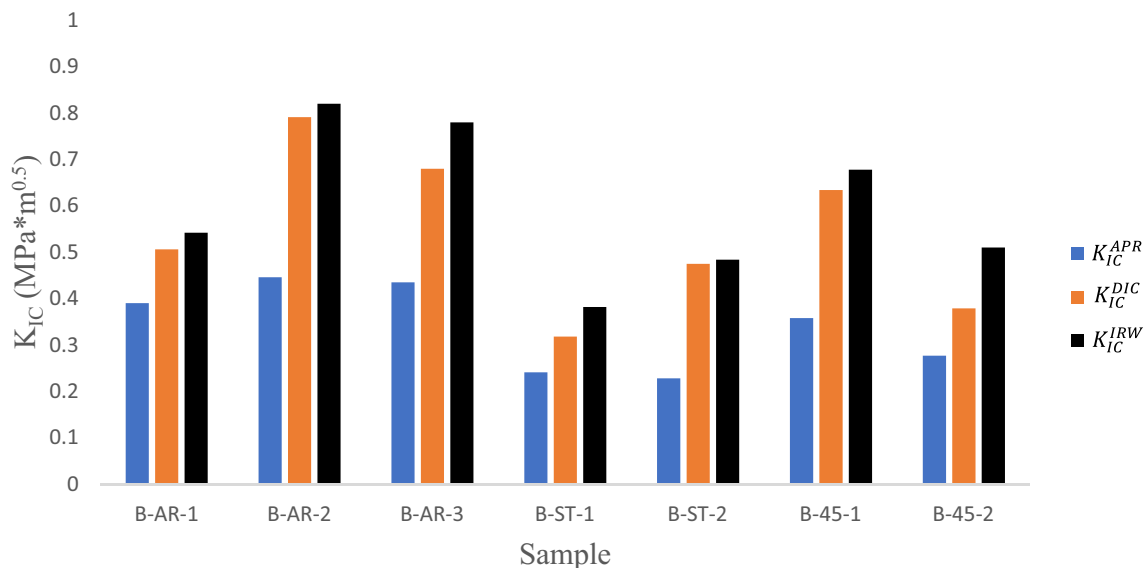
$K_{\text{IC}}^{\text{APR}}$ is more than 26% lower than $K_{\text{IC}}^{\text{IRW}}$. Exact fracture toughness values for both charts can be seen in Table 7. Average $K_{\text{IC}}^{\text{IRW}}$ values and average $K_{\text{IC}}^{\text{DIC}}$ values for different orientations are shown in Table 8. Mancos Shale samples have the highest fracture toughness, while samples with arrester orientation show the highest fracture toughness values for both Mancos Shale and Berea Sandstone.

As stated in Sect. 1, stress intensity factor solution using full-field displacement has been developed and used for materials that exhibit perfectly linear elastic behavior. Currently, there is no available literature to prove validity of this method for rocks or other materials that exhibit large FPZ. However, this study shows that if optimum area of interest, field of view and number of terms in solution are selected, DIC solution can provide a good match with fracture toughness values obtained using Irwin's approach for inelastic zone correction.

5 Conclusions

Digital image correlation was integrated with semi-circular bend test to measure mode I fracture toughness of Berea Sandstone and Mancos Shale in different orientations. Effect of parameters of solution on measuring fracture toughness of rocks was examined, allowing to choose for the most suitable ones.

- Displacement fields obtained by the DIC can be used to measure fracture toughness of rocks.

**Fig. 18** Comparison between $K_{\text{IC}}^{\text{APR}}$, $K_{\text{IC}}^{\text{DIC}}$, and $K_{\text{IC}}^{\text{IRW}}$ values for Berea Sandstone

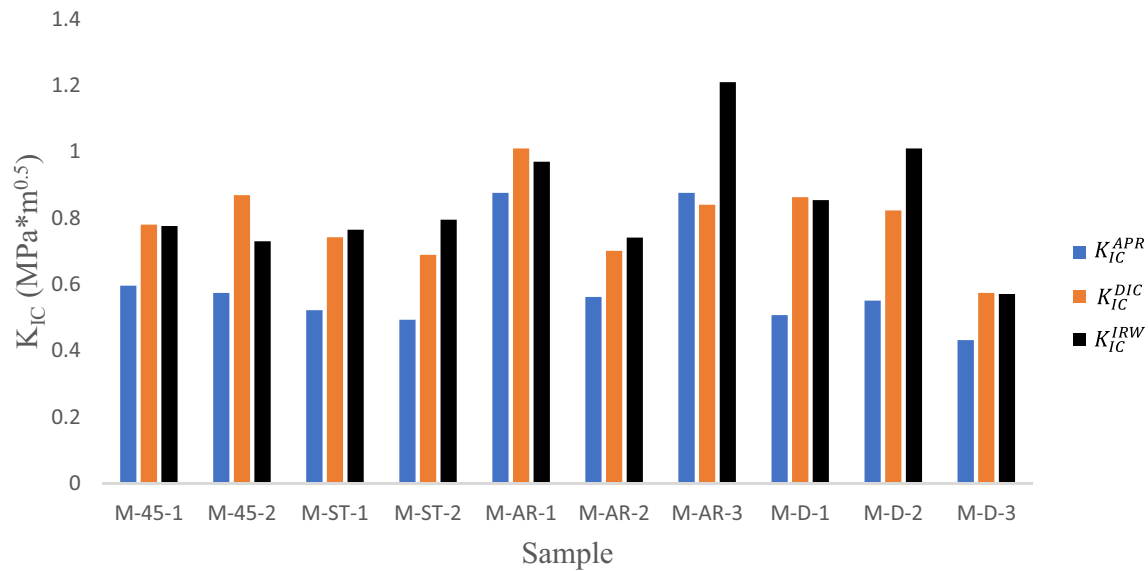


Fig. 19 Comparison between K_{IC}^{APR} , K_{IC}^{DIC} , and K_{IC}^{IRW} values for Mancos Shale

Table 7 Comparison of K_{IC}^{APR} , K_{IC}^{IRW} , and K_{IC}^{DIC} for all samples

	K_{IC}^{APR} (MPa \times m $^{0.5}$)	K_{IC}^{IRW} (MPa \times m $^{0.5}$)	K_{IC}^{DIC} (MPa \times m $^{0.5}$)
Berea			
B-AR-1	0.390	0.542	0.506
B-AR-2	0.446	0.820	0.791
B-AR-3	0.435	0.780	0.680
B-ST-1	0.241	0.382	0.318
B-ST-2	0.228	0.484	0.475
B-45-1	0.358	0.678	0.634
B-45-2	0.277	0.510	0.379
Mancos			
M-45-1	0.596	0.776	0.780
M-45-2	0.574	0.730	0.869
M-ST-1	0.522	0.765	0.742
M-ST-2	0.493	0.795	0.689
M-AR-1	0.876	0.970	1.010
M-AR-2	0.562	0.741	0.701
M-AR-3	0.876	1.210	0.840
M-D-1	0.507	0.854	0.863
M-D-2	0.551	1.010	0.823
M-D-3	0.432	0.571	0.574

Table 8 Average K_{IC}^{IRW} and K_{IC}^{DIC} for samples in tested orientations

Formation	Orientation	K_{IC}^{IRW} (MPa \times m $^{0.5}$)	K_{IC}^{DIC} (MPa \times m $^{0.5}$)
Mancos	AR	0.973	0.850
Mancos	45	0.753	0.824
Mancos	ST	0.780	0.715
Mancos	D	0.811	0.753
Berea	AR	0.714	0.659
Berea	45	0.594	0.506
Berea	ST	0.433	0.396

- “Full” area of interest, N of 10, and more and FOV of 52×39 mm 2 will provide the most accurate results in measuring fracture toughness of geologic materials.
- Results obtained from SCB test need to be corrected for FPZ. FPZ can be tracked and quantified using DIC.

- Average FPZ size for Berea Sandstone is 4.9 ± 1.1 mm and for Mancos Shale average FPZ size is 2.3 ± 0.9 .
- For Berea Sandstone, average K_{IC}^{DIC} values are 0.659 MPa \times m $^{0.5}$ in arrester orientation, 0.506 MPa \times m $^{0.5}$ in 45° and 0.396 MPa \times m $^{0.5}$ in short transverse orientation. Average K_{IC}^{IRW} values are 0.714 MPa \times m $^{0.5}$ in arrester orientation, 0.594 MPa \times m $^{0.5}$ in 45° orientation, and 0.433 MPa \times m $^{0.5}$ in short transverse orientation.
- For Mancos Shale, average K_{IC}^{DIC} values are 0.850 MPa \times m $^{0.5}$ in arrester orientation, 0.824 MPa \times m $^{0.5}$ in 45°, 0.715 MPa \times m $^{0.5}$ in short transverse orientation, and 0.753 MPa \times m $^{0.5}$ in divider orientation. Average K_{IC}^{IRW} values are 0.973 MPa \times m $^{0.5}$ in arrester orientation, 0.753 MPa \times m $^{0.5}$ in 45° orientation, 0.780 MPa \times m $^{0.5}$ in short transverse orientation, and 0.816 MPa \times m $^{0.5}$ in divider orientation.

- Corrected values and values obtained using DIC are in a good match—the results are within 10.5% for Berea Sandstone and 9.6% for Mancos Shale.

Acknowledgements The authors are grateful to Mr. Mark LeBlanc, Philip Wortman, Archie Metoyer, and Donatien-Roland Diby for their help in sample preparation and experimental setup. The authors are also grateful to Tuscaloosa Marine Shale Research Group for their feedback and support. This material is based upon work supported by the Department of Energy National Energy Technology Laboratory under Award Number DE-FE0031575 (TUSCALOOSA MARINE SHALE LABORATORY).

Funding This material is based upon work supported by the Department of Energy National Energy Technology Laboratory under Award Number DE-FE0031575.

Data Availability All data were obtained from the experiments conducted by the authors.

Compliance with Ethical Standards

Conflict of Interest None.

Consent to Participate All authors consented to participate in this work.

Consent for Publication All authors consent for this work to be published.

References

- Aliha MRM, Ayatollahi MR, Akbardoost J (2012) Typical upper bound-lower bound mixed mode fracture resistance envelopes for rock material. *Rock Mech Rock Eng* 45:65–74. <https://doi.org/10.1007/s00603-011-0167-0>
- Al-Shayea NA (2002) Comparing reservoir and outcrop specimens for mixed mode I-II fracture toughness of a limestone rock formation at various conditions. *Rock Mech Rock Eng* 35(4):271–297. <https://doi.org/10.1007/s00603-002-0027-z>
- Al-Shayea NA (2005) Crack propagation trajectories for rocks under mixed modes I-II fracture. *Eng Geol* 81(1):84–97. <https://doi.org/10.1016/j.enggeo.2005.07.013>
- Anderson TL (2005) *Fracture mechanics: fundamentals and applications*, 3rd edn. CRC Press, Boca Raton, FL
- Ayatollahi MR, Nejati M (2011) An over-deterministic method for calculation of coefficients of crack tip asymptotic field from finite element analysis. *Fatigue Fract Eng Mater Struct* 34:159–176. <https://doi.org/10.1111/j.1460-2695.2010.01504.x>
- Ayatollahi MR, Akbardoost J (2012) Size effects on fracture toughness of quasi-brittle materials—a new approach. *Eng Fract Mech* 92:89–100. <https://doi.org/10.1016/j.engfractmech.2012.06.005>
- Ayatollahi MR, Akbardoost J (2013a) Size and geometry effects on rock fracture toughness: mode I fracture. *Rock Mech Rock Eng* 47:677–687. <https://doi.org/10.1007/s00603-013-0430-7>
- Ayatollahi MR, Akbardoost J (2013b) Size effects in mode II brittle fracture of rocks. *Eng Fract Mech* 112–113:165–180. <https://doi.org/10.1016/j.engfractmech.2013.10.011>
- Barree RD, Conway MW, Gilbert JV, Woodroof RA (2010) Evidence of strong fracture height containment based on complex shear failure and formation anisotropy. In: Paper presented at SPE annual technical conference and exhibition, Florence, Italy
- Bazant ZP, Kim J-K, Pfeiffer PA (1986) Nonlinear fracture properties from size effect tests. *J Struct Eng* 112(2):289–307. [https://doi.org/10.1061/\(ASCE\)0733-9445\(1986\)112:2\(289\)](https://doi.org/10.1061/(ASCE)0733-9445(1986)112:2(289))
- Bazant ZP, Gettu R, Kazemi MT (1991) Identification of nonlinear fracture properties from size effect tests and structural analysis based on geometry-dependent R-curves. *Int J Rock Mech Mining Sci Geomech Abstr* 28(1):43–51. [https://doi.org/10.1016/0148-9062\(91\)93232-U](https://doi.org/10.1016/0148-9062(91)93232-U)
- Chandler M, Meredith P, Brantut N, Crawford B (2016) Fracture toughness anisotropy in shale. *J Geophys Res: Solid Earth*. <https://doi.org/10.1002/2015JB012756>
- Chang SH, Lee CI, Jeon S (2002) Measurement of rock fracture toughness under modes I and II and mixed-mode conditions by using disc-type specimens. *Eng Geol* 66(1–2):79–97. [https://doi.org/10.1016/S0013-7952\(02\)00033-9](https://doi.org/10.1016/S0013-7952(02)00033-9)
- Chong KP, Kuruppu MD (1984) New specimen for fracture toughness determination of rock and other materials. *Int J Fract* 26(2):59–62. <https://doi.org/10.1007/BF01157555>
- Dong W, Yang D, Zhou X, Kastiukas G, Zhang B (2017) Experimental and numerical investigations on fracture process zone of rock–concrete interface. *Fatigue Fract Eng Mater Struct* 40(5):820–835. <https://doi.org/10.1111/ffe.12558>
- Dyskin AV (1997) Crack growth criteria incorporating non-singular stresses: size effect in apparent fracture toughness. *Int J Fract* 83:191–206. <https://doi.org/10.1023/A:1007304015524>
- Forbes Inskip ND, Meredith PG, Chandler MR, Gudmundsson A (2018) Fracture properties of nash point shale as a function of orientation to bedding. *J Geophys Res: Solid Earth* 123:8428–8444. <https://doi.org/10.1029/2018JB015943>
- Fowell RJ (1995) Suggested method for determining mode I fracture toughness using cracked chevron notched Brazilian disc (CCNBD) specimens. *Int J Rock Mech Mining Sci Geomech Abstr* 32(1):57–64. [https://doi.org/10.1016/0148-9062\(94\)00015-U](https://doi.org/10.1016/0148-9062(94)00015-U)
- Gao G, Huang S, Xia K, Li Z (2015) Application of digital image correlation (DIC) in dynamic notched semi-circular bend (NSCB) tests. *Exp Mech* 55(1):95–104. <https://doi.org/10.1007/s11340-014-9863-5>
- Gokaraju D, Govindarajan S, Mitra A, Aldin M, Patterson R (2017) Evaluation of fracture toughness and its impact on hydraulic fracturing. In: Paper presented at the 51st US Rock Mechanics/Geomechanics Symposium. American Rock Mechanics Association, San-Francisco, California
- Good practices guide for digital image correlation (2018) International digital image correlation society. http://www.idics.org/guide/GoodPracticeIntroduction_2018.V2brief.pdf. Accessed 25 Dec 2019
- Guo ZK, Kobayashi A (1993) Further studies on fracture process zone for mode I concrete fracture. *Eng Fract Mech* 46(6):1041–1049. [https://doi.org/10.1016/0013-7944\(93\)90155-L](https://doi.org/10.1016/0013-7944(93)90155-L)
- Irwin GR (1961) Plastic zone near a crack and fracture toughness. *Sagamore Res Conf Proc* 4:63–78
- Karihaloo BL (1999) Size effect in shallow and deep notched quasi-brittle structures. *Int J Fract* 95:379–390. <https://doi.org/10.1023/A:1018633208621>
- Kennedy A (2011) *Geologic Predictors of the hydrocarbon extraction potential of the Mancos Shale*, PhD Dissertation. University of Utah, Salt Lake City
- Kuruppu MD, Chong KP (2012) Fracture toughness testing of brittle materials using semi-circular bend (SCB) specimen. *Eng Fract Mech* 91:133–150. <https://doi.org/10.1016/j.engfractmech.2012.01.013>
- Kuruppu MD, Obara Y, Ayatollahi MR et al (2013) ISRM-suggested method for determining the mode I static fracture toughness using

- semi-circular bend specimen. *Rock Mech Rock Eng* 47(1):267–274. <https://doi.org/10.1007/s00603-013-0422-7>
- Lee HP, Olson JE, Holder J, Gale JFW, Myers RD (2015) The interaction of propagating opening mode fractures with preexisting discontinuities in shale. *JGR Solid Earth* 120(1):169–181. <https://doi.org/10.1002/2014JB011358>
- Lim IL, Johnston IW, Choi SK (1993) Stress intensity factors for semi-circular specimens under three-point bending. *Eng Fract Mech* 44(3):362–382. [https://doi.org/10.1016/0013-7944\(93\)90030-V](https://doi.org/10.1016/0013-7944(93)90030-V)
- Lim IL, Johnston IW, Choi SK, Boland JN (1994a) Fracture testing of a soft rock with semi-circular specimens under three-point bending. Part 1—mode I. *Int J Rock Mech Mining Sci Geomech Abstr* 31(3):185–197. [https://doi.org/10.1016/0148-9062\(94\)90463-4](https://doi.org/10.1016/0148-9062(94)90463-4)
- Lim IL, Johnston IW, Choi SK, Boland JN (1994b) Fracture testing of a soft rock with semi-circular specimens under three-point bending. Part 2—mixed-mode. *Int J Rock Mech Mining Sci Geomech Abstr* 31(3):199–212. [https://doi.org/10.1016/0148-9062\(94\)90464-2](https://doi.org/10.1016/0148-9062(94)90464-2)
- Lin Q, Labuz JF (2013) Fracture of sandstone characterized by digital image correlation. *Int J Rock Mech Min Sci* 60:235–245. <https://doi.org/10.1016/j.ijrmms.2012.12.043>
- McNeill SR, Peters WH, Sutton MA (1987) Estimation of stress intensity factor by digital image correlation. *Eng Fract Mech* 28(1):101–112. [https://doi.org/10.1016/0013-7944\(87\)90124-X](https://doi.org/10.1016/0013-7944(87)90124-X)
- Meredith PG (1989) Comparative fracture toughness testing of rocks. In: *Fracture toughness and fracture energy: test methods for concrete and rock*. Brookfield, Rotterdam, pp 265–278
- Mikhailsevitch V, Lebedev M, Gurevich B (2016) A laboratory study of the elastic anisotropy in the Mancos Shale at seismic frequencies. *SEG Technical Program Extended Abstracts*: 3174–3178. <https://doi.org/10.1190/segam2016-13850199.1>
- Mokhtarishirazabad M, Lopez-Crespo P, Moreno B, Lopez-Moreno A, Zanganeh M (2016) Evaluation of crack-tip fields from DIC data: a parametric study. *Int J Fatigue* 89:11–19. <https://doi.org/10.1016/j.ijfatigue.2016.03.006>
- Nath F, Mokhtari M (2018) Optical visualization of strain development and fracture propagation in laminated rocks. *J Petrol Sci Eng* 167:354–365. <https://doi.org/10.1016/j.petrol.2018.04.020>
- Nejati M, Dambly MLT, Saar MO (2019) A methodology to determine the elastic properties of anisotropic rocks from a single uniaxial compression test. *J Rock Mech Geotech Eng* 11(6):1166–1183. <https://doi.org/10.1016/j.jrmge.2019.04.004>
- Ramos MJ, Espinoza DN, Torres-Verdin C, Grover T (2017) Use of shear-wave anisotropy to quantify the onset of stress-induced microfracturing. *Geophysics*. <https://doi.org/10.1190/geo2016-0579.1>
- Ramos MJ, Espinoza DN, Goldfarb EJ, Tisato N, Laubach SE, Torres-Verdin C (2018) Microstructural controls on elastic anisotropy of finely laminated Mancos shale. *Geophys J Int* 216(2):991–1004. <https://doi.org/10.1093/gji/ggy474>
- Sanford RJ, Dally JW (1979) A general method for determining mixed-mode stress intensity factors from isochromatic fringe patterns. *Eng Fract Mech* 11(4):621–633. [https://doi.org/10.1016/0013-7944\(79\)90123-1](https://doi.org/10.1016/0013-7944(79)90123-1)
- Schmidt RA (1980) A microcrack model and its significance to hydraulic fracturing and fracture toughness testing. In: *Presented at the 21st US symposium on rock mechanics (USRMS)*, Rolla, Missouri
- Thiercelin M (1989) Fracture toughness and hydraulic fracturing. *Int J Rock Mech Mining Sci Geomech* 26(3–4):177–183. [https://doi.org/10.1016/0148-9062\(89\)91967-0](https://doi.org/10.1016/0148-9062(89)91967-0)
- Tutluoglu L, Keles C (2011) Mode I fracture toughness determination with straight notched disk bending method. *Int J Rock Mech Min Sci* 48(8):1248–1261. <https://doi.org/10.1016/j.ijrmms.2011.09.019>
- Wang H, Zhao F, Huang Z, Yao Y, Yuan G (2017) Experimental study of mode-I fracture toughness for layered shale based on two ISRM-suggested methods. *Rock Mech Rock Eng* 50:1933–1939. <https://doi.org/10.1007/s00603-017-1180-8>
- Wei MD, Dai F, Xu NW, Zhao T, Xia KW (2016) Experimental and numerical study on the fracture process zone and fracture toughness determination for ISRM-suggested semi-circular bend rock specimen. *Eng Fract Mech* 154:43–56. <https://doi.org/10.1016/j.engfracmech.2016.01.002>
- Yoneyama S, Ogawa T, Kobayashi Y (2007) Evaluating mixed-mode stress intensity factors from full-field displacement fields obtained by optical methods. *Eng Fract Mech* 74(9):1399–1412. <https://doi.org/10.1016/j.engfracmech.2006.08.004>
- Yu Y, Zeng W, Liu W, Zhang H, Wang X (2019) Crack Propagation and fracture process zone (FPZ) of wood in the longitudinal direction determined using digital image correlation (DIC) technique. *Remote Sens* 11(13):1562. <https://doi.org/10.3390/rs11131562>
- Zhang R, He L (2012) Measurement of mixed-mode stress intensity factors using digital image correlation method. *Opt Lasers Eng* 50(7):1001–1007. <https://doi.org/10.1016/j.optlaseng.2012.01.009>
- Zhang H, Fu D, Song H, Kang Y, Huang G, Qi G, Li J (2015) Damage and fracture investigation of three-point bending notched sandstone beams by DIC and AE techniques. *Rock Mech Rock Eng* 48:1297–1303. <https://doi.org/10.1007/s00603-014-0635-4>

Publisher's Note Springer Nature remains neutral with regard to jurisdictional claims in published maps and institutional affiliations.